Advanced Steel Construction – Vol. 22 No. 1 (2026) 8–16
DOI:10.18057/IJASC.2026.22.1.2

PLASTIC ENHANCEMENT OF COLD-FORMED THIN-WALLED STEEL FOR PREFABRICATED SUPPORT AND HANGER

Zong-Lai Peng [1], Yi-Pei Zeng [1], Ning Xu [1], Xian-Hui Yi [1], Fu-Li Liu [1], Wei Xiong [1] and Yong Cai [2, *]

[1] *China Construction Fifth Bureau Installation Engineering Co., LTD, Shenzhen 518118, China*
[2] *School of Civil Engineering, Central South University, Changsha 410075, China*
** (Corresponding author: E-mail: 18803314336@163.com)*

ABSTRACT

In prefabricated support and hanger, the study of corner strength in cold-formed thin-walled steel (CFTWS) is crucial. Corners are prone to stress concentration, increasing local buckling and connection failure risks. This study analyzes the stress in the corner parts and derives the yield strength using the linear hardening model and the Von-Mises yield criterion. Based on the Prandtl-Reuss flow rule and strain superposition principle in plastic mechanics, a theoretical analysis of corner material hardening during the cold-bending process is conducted. Experiments and ABAQUS simulations are carried out to prove the effectiveness of the theoretical model. The findings reveal that the cold bending effect is relatively significant. The yield strength of the corner parts is about 79-86 MPa higher than that of the flat parts, which is equivalent to an increase of 23% to 25%. Due to the relatively low degree of anisotropy and smaller thickness measurement errors in thicker CFTWS, the theoretical formula has higher calculation accuracy for steel plates with greater thickness. In addition, in the same batch of steel produced by the same cold bending process, the yield strength of CFTWS slightly decreases with the increase of thickness.

ARTICLE HISTORY

Received: 14 March 2025
Revised: 27 June 2025
Accepted: 2 July 2025

KEYWORDS

Prefabricated support and hanger;
Cold-formed thin-walled steel;
Yield strength;
Linear hardening model;
Corner parts

1. Introduction

As prefabricated construction is advancing and popularizing swiftly on a global scale, the construction industry is undergoing a technological revolution aimed at improving construction efficiency, reducing costs, and minimizing environmental impact. The core advantage of prefabricated construction lies in its modular and factory-based production characteristics, which not only accelerate construction progress but also help achieve standardization of building quality and performance [1-4]. In prefabricated support and hanger, examining the corner strength of CFTWS is vital. Corners are susceptible to stress concentration, heightening the risk of local buckling and connection failures. Studying this aspect aids in comprehending stress distribution, thereby facilitating optimized structural design and augmenting load-bearing capacity and stability.

Fig. 1 shows common prefabricated support and hanger used in subway and housing construction. CFTWS, with its ability to achieve complex cross-sectional shapes during processing, perfectly fits the customized needs of prefabricated support and suspension systems. The lightweight, high-strength, and good processing performance of this material make it an ideal choice for prefabricated support and hanger [5-7], meeting the modern construction requirements for rapid construction and high load-bearing capacity. However, to further enhance its performance in practical applications, in-depth research on the plastic strengthening of CFTWS is particularly necessary.

Fig. 1 CFTWS in prefabricated support and hanger

While cold bending is taking place, the steel endures plastic deformation, which leads to changes in the material's crystal lattice structure, thereby requiring greater stress to continue plastic deformation under subsequent loading. This effect is referred to as strain hardening or plastic strengthening, which increases the material's yield strength. In CFTWS, research on plastic strengthening involves the material's yield criteria and plastic stress-strain relationships [8-10]. This paper aims to explore the research on plastic strengthening in this field, discussing it from three aspects: theoretical research, numerical simulation, and experimental research, to highlight its key role in static design and application.

Up to now, some studies on plastic strengthening and residual stress during the cold bending of metals have mainly focused on carbon steel sections [11-13] and stainless steel sections [14-16], with some representative work among them. Wang et al. [17] studied the link between cold deformation and mechanical parameters of 316L austenitic stainless steel. Their work found that cold working somewhat raises the material's yield stress but doesn't significantly affect the reduction factor. Byun et al. [18] studied the true strain hardening and plastic instability characteristics of steel at different test temperatures. The strength decreased with increasing temperature in both annealed and cold-worked states, while plasticity reached a peak below room temperature. In high-temperature conditions, work-hardened samples failed via instantaneous necking once their yield stress surpassed the plastic instability stress. Ghosh et al. [19] explored how plastic deformation from cold rolling or surface processing affects the chloride - induced stress corrosion cracking susceptibility of 304L austenitic stainless steel at ambient temperature. Test materials underwent solution annealing, cold rolling, and surface processing to create varying material strain and stress levels. The results showed that cracks in the cold-worked samples propagated along slip lines and cracked earlier than the solution-annealed samples. Kim et al. [20] compared steel's deformation mechanisms and mechanical properties at different temperatures. The 293 K tensile curve showed a smooth elastic-plastic transition with continuous work hardening. In contrast, the 123 K curve exhibited yield point extension, strain softening, followed by sudden strain hardening and fracture.

As early as 1997, Macdonald et al. [21] used standard hardness testing

methods to determine the local yield strength at the cold-formed corners. Compared with the design specification methods, using hardness measurement to estimate material strength achieved the main goal of collecting detailed mapping of the distribution of yield stress increases due to cold working. It was also pointed out that the yield values from hardness testing can be used to conservatively estimate the increase in yield stress of cold-formed sections.

In the past decade or so, cold bending technology has increasingly gained attention due to its unique advantages, stimulating the research enthusiasm of many scholars who have turned their research focus to the field of CFTWS. With the popularization and maturation of cold bending processes, its potential for application in the fields of construction and engineering has gradually been explored, attracting in-depth academic exploration of its performance and applications. Ungureanu et al. [22] based on some of the latest surveys and collected literature data, took inventory and classified local plastic mechanisms, providing the ultimate load-bearing capacity of some of the most commonly used cold-bent steel structure sections. Yao et al. [23] developed a finite-element-based method to predict residual stress and equivalent strain distribution in cold-bent steel hollow profiles. This method effectively simulates these distributions, which are hard to measure in labs. Later, simplified models for residual stress and equivalent strain in cold-bent steel elliptical hollow sections were proposed [24]. These models aid in defining component initial states for nonlinear finite element analysis, helping future research assess cold-working effects on component behavior. Luo et al. [25] examined how material strength, plate thickness, sampling position, and heating temperature affect the post - fire mechanical properties of CFTWS. Their study found that exposure to 800°C could reduce yield strength by 40%. However, cold-worked strain hardening can still increase yield strength by 20%. Kim et al. [26] investigated the mechanical properties of cold-bent and heat-treated pipe elbows by conducting tensile tests on simulated samples. The study found that despite heat treatment to eliminate residual stress, the strength of cold-worked material is higher than that of the parent material, while plasticity is lower. The increase in strength and the decrease in plasticity are proportional to the strain level applied during the cold working process. Korsun et al. [27] noted the mechanical properties' non - uniform section - wide distribution in the profile, as hardening in the bending corners and adjacent areas boosts metal strength. Analysis of thin steel plate samples with and without hardening effects showed that the maximum stress in non-hardened samples was more than 30% higher than that in hardened samples, and the maximum displacement in the hardened state was more than triple. Gao et al. [28] performed finite-element parametric analyses using manually calculated residual stress and plastic strain, probing cold bending's impact on steel columns' response. Compared to cases ignoring cold-bending effects, models with isotropic hardening raise the apparent yield stress and column load-bearing capacity.

However, most existing studies on CFTWS focus on the overall performance and processing of the material. These studies lack an in-depth analysis of the plastic strengthening characteristics of the corners, which limits the full utilization of the potential of CFTWS in prefabricated support and hanger. The corners, as key areas for connection and load-bearing in support and hanger, are crucial for improving the stability and load-bearing capacity. Research on the plastic strengthening of CFTWS for prefabricated support and hanger is of significant theoretical and practical importance in the field of statics. This will not only provide theoretical support for the design of prefabricated support and hanger but also promote the performance optimization and innovative design of CFTWS in a wider range of engineering applications, thus providing new perspectives and solutions for the application of CFTWS in the field of prefabricated construction.

The layout of this paper is presented as follows: Section 2 provides a theoretical analysis of cold bending process, focusing on the elastoplastic constitutive relationship. In Section 3, we conduct an examination of the stress distribution at the corners of CFTWS sections and develop a formula for calculating the yield strength at these corners using the Von-Mises yield criterion. Section 4 conducts tensile tests on two types of CFTWS, including the corner parts and flat plate parts, comparing the experimentally measured yield strength with theoretical values. Section 5 combines the constitutive relationships obtained from the experiments with ABAQUS software for analysis, comparing the obtained failure modes with the experiments. Finally, some conclusions are summarized in Section 6.

2. Theoretical analysis of cold bending process

Forming thin-walled steel sections via cold bending mainly involves elastic-plastic deformation of the steel plates. As a numerical computational method for analyzing the elastic and plastic deformations of materials under external forces, the elastoplastic finite element method serves as a theoretical tool for analyzing the cold bending forming process. Unlike elastic deformation, the plastic deformation during the cold bending process is irreversible, and the superposition principle no longer applies. In the plastic development zone, when the stress exceeds the yield limit, irreversible changes begin to occur within the material's microstructure, complicating the stress-strain relationship, which no longer conforms to Hooke's law. During plastic deformation, the stress-strain relationship of the material depends not only on the current stress and strain states but is also significantly influenced by the loading history. This means that even at the same stress level, different loading paths and histories can lead to different strain responses.

According to plasticity theory, the stress-strain tensor can be split into spherical and deviatoric parts. The spherical tensor represents the average effect of the stress tensor, that is, the hydrostatic pressure, which is related to volume changes in the material and does not cause shape changes. Yield criteria are usually defined based on the deviatoric tensor to determine whether the material has entered the plastic state.

For isotropic materials, the internal structure is uniform and identical in all directions. Therefore, the yield behavior of such materials is not affected by the orientation of the coordinate axes; that is, no matter the direction of the stress, as long as the stress magnitude and combination are the same, the material's response will be the same. In this case, the yield function of the material can be represented by three principal stresses（$\sigma_1 \geq \sigma_2 \geq \sigma_3$）, as the principal stresses represent the maximum, intermediate, and minimum stresses in three orthogonal directions. Thus, the yield function

$$f(\sigma_1,\sigma_2,\sigma_3)=0 \tag{1}$$

As shown in Fig. 2, since the yield curve under the Von-Mises condition is the circumcircle of the Tresca hexagon, the yield function can be derived as follows

$$\frac{1}{2}\left[(\sigma_1-\sigma_2)^2+(\sigma_2-\sigma_3)^2+(\sigma_3-\sigma_1)^2\right]=k^2 \tag{2}$$

Where, k is a constant associated with the base material. It can be determined through a simple tension test, as the yield criterion is applicable to various stress states. During simple tension, we have

$$k=\sigma_s \tag{3}$$

Where, σ_s represents the yield stress of the base material.

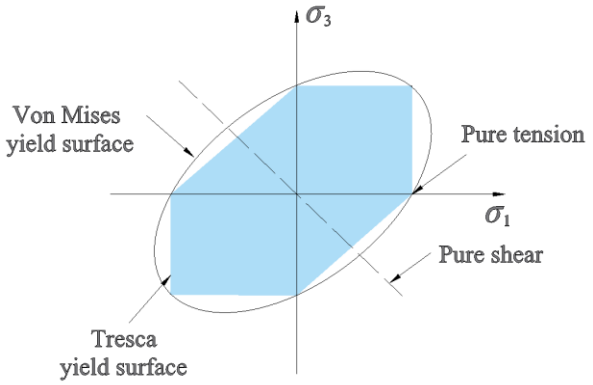

Fig. 2 The connection between Von-Mises criterion and Tresca criterion

According to the calculation formula for stress intensity, it has the following relationship with the octahedral shear stress:

$$\bar{\sigma}=\frac{3\sqrt{2}}{2}\tau_{oct} \tag{4}$$

Where, τ_{oct} represents the octahedral shear stress, and its calculation formula is:

$$\tau_{oct}=\frac{1}{3}\sqrt{(\sigma_1-\sigma_2)^2+(\sigma_2-\sigma_3)^2+(\sigma_3-\sigma_1)^2} \tag{5}$$

According to the Von-Mises condition [29], when the stress intensity reaches a certain value, the material begins to enter the plastic state.

$$\bar{\sigma} = k \tag{6}$$

Combining Eqs. (3) and (6), we can obtain

$$\bar{\sigma} = \sigma_s \tag{7}$$

The Von-Mises yield criterion indicates that when the equivalent stress equals the tensile yield limit, the material starts to plastically deform. Between the elastic and plastic zones of the material, as well as between the loading and unloading zones, there exists a transition zone (neutral zone). Within this zone, the material exhibits both elastic and plastic characteristics. To ensure the continuity of stress and strain in the neutral zone, the plastic relationship should automatically revert to the elastic relationship within the neutral zone. Incremental theory can guarantee this continuity, but total theory cannot. However, under conditions of small deformations and simple loading, the two theories are consistent, meaning that the total relationship can be derived from the incremental relationship. For cold bending forming, there is a neutral zone that needs to ensure its continuity, and since nonlinear finite elements mainly use plastic incremental theory, it is reasonable to use incremental theory in the cold bending forming process.

According to the Prandtl-Reuss flow rule,

$$\mathrm{d}\varepsilon_{ij}^{\mathrm{p}} = \mathrm{d}\lambda S_{ij},\ \mathrm{d}\lambda \geq 0 \tag{8}$$

Where, $\mathrm{d}\lambda$ represents the proportionality factor, which is related to the position of the material point and the level of load, hence the equation above is a nonlinear relationship. $\mathrm{d}\varepsilon_{ij}^{\mathrm{p}}$ denotes the increment of plastic strain, and S_{ij} represents the deviatoric stress tensor, satisfying

$$S_{ij} = \frac{\partial p_{\mathrm{f}}}{\partial \sigma_{ij}} \tag{9}$$

Where, p_{f} represents the loading function, and σ_{ij} represents the stress components.

According to the principle of superposition of strains, the total strain increment during the cold bending forming process is composed of the elastic strain increment and the plastic strain increment, that is:

$$\mathrm{d}\varepsilon_{ij} = \mathrm{d}\varepsilon_{ij}^{\mathrm{e}} + \mathrm{d}\varepsilon_{ij}^{\mathrm{p}} \tag{10}$$

In elastoplastic deformation, the stress increment caused by the elastic strain increment obeys Hooke's law and can be expressed as

$$\mathrm{d}\sigma_{ij}^{e} = D^{\mathrm{e}}\mathrm{d}\varepsilon_{ij}^{e} \tag{11}$$

Where, D^{e} represents the elastic modulus matrix.

Stress and strain satisfy the following expression:

$$\mathrm{d}\sigma_{ij} = D^{\mathrm{ep}}\mathrm{d}\varepsilon_{ij} \tag{12}$$

Where, D^{ep} represents the elastoplastic matrix. And the following relationship holds:

$$D^{\mathrm{ep}} = D^{\mathrm{e}} - D^{\mathrm{p}} \tag{13}$$

$$D^{\mathrm{p}} = \frac{D^{\mathrm{e}}}{\Omega} - \frac{\partial p_{\mathrm{f}}}{\partial \sigma_{ij}}\left(D^{\mathrm{e}}\frac{\partial p_{\mathrm{f}}}{\partial \sigma_{ij}}\right)^{\mathrm{T}} \tag{14}$$

$$\Omega = \left(\frac{\partial p_{\mathrm{f}}}{\partial \sigma_{ij}}\right)^{\mathrm{T}} D^{\mathrm{e}}\frac{\partial p_{\mathrm{f}}}{\partial \sigma_{ij}} - \frac{\partial p_{\mathrm{f}}}{\partial K}\left(\frac{\partial K}{\partial \varepsilon_{ij}^{\mathrm{p}}}\right)^{\mathrm{T}}\frac{\partial p_{\mathrm{f}}}{\partial \sigma_{ij}} - \left(\frac{\partial p_{\mathrm{f}}}{\partial \varepsilon_{ij}^{\mathrm{p}}}\right)^{\mathrm{T}}\frac{\partial p_{\mathrm{f}}}{\partial \sigma_{ij}} \tag{15}$$

Where, Ω is a coefficient matrix related to plastic behavior, and K is a parameter associated with material hardening.

3. Corner yield stress

To simplify the model and facilitate theoretical analysis, the following basic assumptions are introduced:

(1) Plane strain assumption [30], meaning that the strain component perpendicular to the analysis plane is zero.

(2) Linear hardening assumption [31], meaning that the post-yield behavior of the material is considered linear, i.e., after the yield point, the material's stress increases proportionally with strain until the ultimate strength is reached.

(3) Incompressibility assumption [32] in plastic deformation.

(4) Ignoring residual stress [33], time-dependent effects [34], and Bauschinger effects [35].

(5) The elastic strain is much smaller compared to the plastic strain and can be neglected.

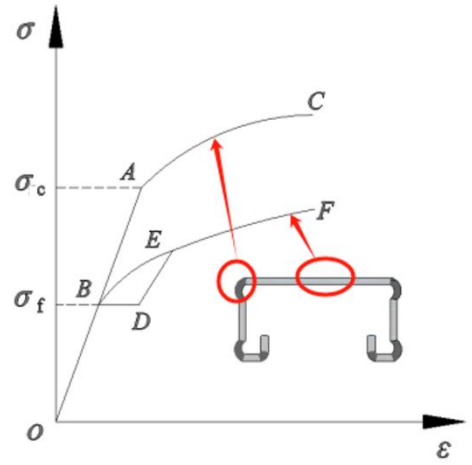

Fig. 3 Stress-strain curves of various parts of CFTWS sections

CFTWS sections are divided into two parts: the corner part and the flat plate part, as shown in Fig. 3.

Cold bending causes plastic deformation, leading to work hardening and higher material yield strength [36]. If shear stress is neglected [37-39], the stress analysis problem can be considered as an axisymmetric problem, as shown in Fig. 4.

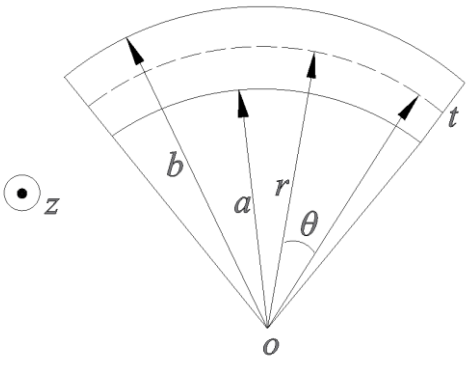

Fig. 4 Axisymmetric bending of the corner section

In Fig. 4, a represents the distance from the inner surface of the cylinder to the center, b represents the distance from the outer surface of the cylinder to the center, r is the displacement in the radial direction, and θ is the tangential displacement.

According to the Von-Mises criterion, the yield stress at each point in the corner is equal to the effective stress. Since shear stress in multiaxial stress states increases material deformation, thereby increasing effective stress, neglecting shear stress underestimates the actual stress state that the material withstands. Therefore, the calculated effective stress will be less than the actual

value, making the theoretical analysis conservative.

$$\frac{\sigma_\theta-\sigma_r}{2\mu\varepsilon_\theta}=\frac{\sigma_\theta-\sigma_z}{\mu\varepsilon_\theta}=\frac{\sigma_z-\sigma_r}{\mu\varepsilon_\theta}=1 \tag{16}$$

Where, σ_θ, σ_r, σ_z represent the strains along the circumferential, radial, and axial axes, respectively, ε_θ is the strain in the circumferential direction. μ is the material's strength parameter, and the following equation is also valid.

$$\bar{\sigma}=\frac{3}{2}\mu\bar{\varepsilon} \tag{17}$$

Where, $\bar{\sigma}$ and $\bar{\varepsilon}$ represent the effective stress and effective strain, respectively, and the following two relations hold true [40]

$$\bar{\sigma}=\sqrt{\frac{1}{2}[(\sigma_\theta-\sigma_r)^2+(\sigma_\theta-\sigma_z)^2+(\sigma_z-\sigma_r)^2]},\bar{\varepsilon}=\sqrt{\frac{2}{3}(\varepsilon_r^{\,2}+\varepsilon_\theta^{\,2}+\varepsilon_z^{\,2})} \tag{18}$$

Substituting Eq. (16) into Eq. (18) yields:

$$\bar{\sigma}=\begin{cases}\sqrt{3}\mu\varepsilon_\theta,\varepsilon_\theta\geq 0\\ -\sqrt{3}\mu\varepsilon_\theta,\varepsilon_\theta<0\end{cases} \tag{19}$$

In pure bending, there is no shear stress on the cross-section, and the plane section assumption can be used [41]. For any point on the corner part of the section, let the distance to the neutral axis be r, and r_0 be the radius of curvature of the length-unchanged surface. Since strain is proportional to distance, this relationship can be described by the following function:

$$r=r_0e^{\varepsilon_\theta} \tag{20}$$

Taking the element of the corner part for force analysis, the stress components in the cylindrical coordinate system are depicted in Fig. 5.

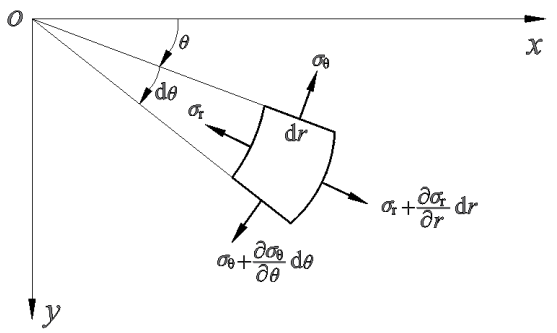

Fig. 5 Stress analysis of the corner element

From the equilibrium differential equation of the element, we get:

$$\frac{\partial\sigma_r}{\partial r}+\frac{\sigma_r-\sigma_\theta}{r}=0 \tag{21}$$

Assuming that the pressure q is acting in the radial direction on the inner surface. According to the force boundary conditions:

$$\sigma_r=\begin{cases}0,\ r=b\\ -q,\ r=a\end{cases} \tag{22}$$

Taking the limit of uniform strain as

$$\Delta=2\delta_{10}-\delta_5 \tag{23}$$

Where, δ_{10} and δ_5 represent the elongation ratios for gauge lengths of 10 times and 5 times the diameter, respectively.

Although some studies focus on advanced analysis methods to delve into the nonlinear behavior of structures under complex loading conditions [42-44]. The linear hardening model is a theoretical model that describes the stress-strain relationship of a material during plastic deformation. In this model, the expression can be written as

$$\bar{\sigma}=\alpha_0\bar{\varepsilon}+\sigma_s,\ \alpha_0=\frac{(1+\Delta)\sigma_b-\sigma_s}{\ln(1+\Delta)} \tag{24}$$

Where, σ_b is the tensile strength of the base metal flat section, which is the maximum stress that the material can withstand in a tensile experiment. α_0 is the slope of the linear hardening model.

The material in the corner section can be assessed for its yield strength under bending conditions using the Von-Mises yield criterion. The yield stress in the elastic region near the neutral surface does not increase due to bending. The yield stress distribution in the corner section is shown in Fig. 6.

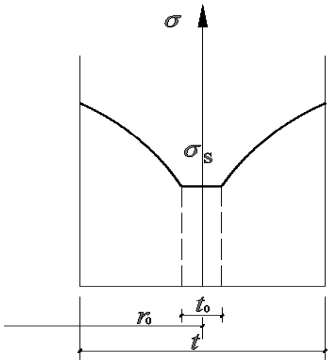

Fig. 6 Distribution of yield stress in the corner section

The yield strength of the corner section of CFTWS is

$$\sigma_c=\frac{2}{b^2-a^2}\left[\int_a^{r_0-\frac{t'}{2}}\bar{\sigma}r\mathrm{d}r+\int_{r_0-\frac{t'}{2}}^{r_0+\frac{t'}{2}}\sigma_s r\mathrm{d}r+\int_{r_0+\frac{t'}{2}}^{b}\bar{\sigma}r\mathrm{d}r\right] \tag{25}$$

Considering the continuity of the radial stress at $r=r_0$, we have:

$$r_0=\sqrt{ab} \tag{26}$$

When the thickness $t_0=0$ of the elastic zone in Fig. 6 under bending, integrating Eq. (25) by parts yields:

$$\sigma_c=\sigma_s+\frac{t}{2a+t}\cdot\frac{(1+\Delta)\sigma_b-\sigma_s}{\sqrt{3}\ln(1+\Delta)} \tag{27}$$

4. Experimental verification

To assess the yield strength and tensile strength of CFTWS in the corner sections, this section conducted tensile tests on two types of CFTWS (41.3mm×41mm×2.0mm and 41.3mm×72mm×2.75mm), including the corner sections and flat plate sections. The corner and flat plate specimens were extracted from the steel profile by milling. Sampling was done according to the "Metallic materials-Method of test at room temperature" (GB/T228-2002) [45].

All specimens were made from the same batch of Q345B grade hot-rolled steel plates that were cold-bent, and the double-limb combined specimens were made by combining single-limb specimens, so only the single-limb specimens were sampled. In the prefabricated support and hanger, the top view plan of the common perforated and non-perforated specimens are shown in Fig. 7.

Specimens are sampled from CFTWS profiles without holes. Sampling positions were at the right-angle and flat plate sections, with the sampling positions and specimen numbers shown in Fig. 8. For specimens with gauge widths of 7.5mm, 10mm, and 15mm, wire cutting was used for processing as

shown in Fig. 9, three specimens were taken for testing at each position.

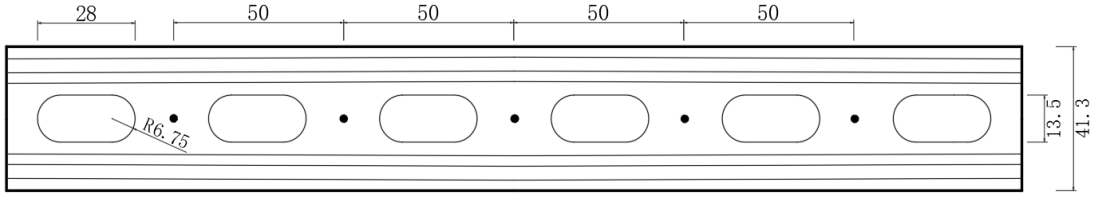

(a) The top view plan of perforated components (mm)

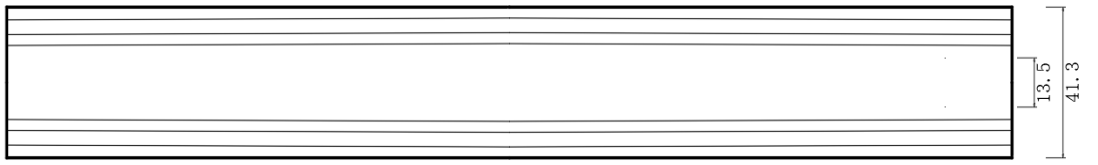

(b) The top view plan of a poreless component (mm)

Fig. 7 The geometric dimensions of the single-limb specimen

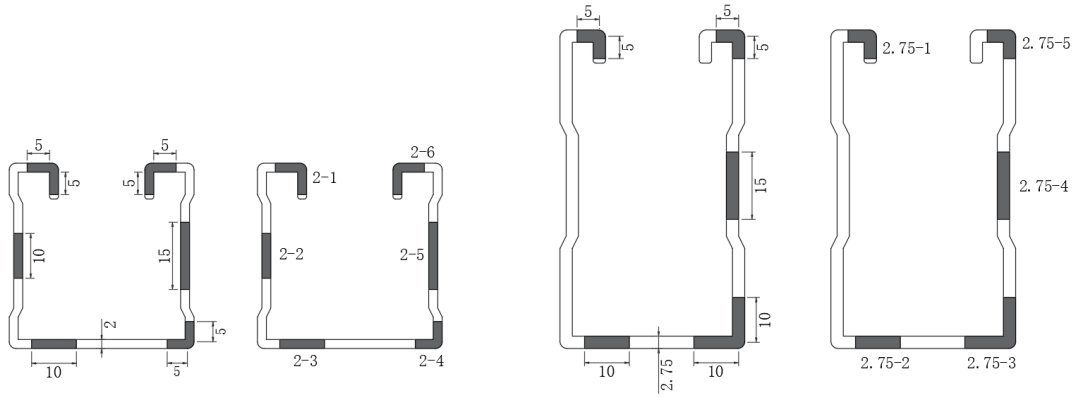

(a) 41.3mm×41mm×2.0mm (b) 41.3mm×72mm×2.75mm

Fig. 8 Sampling positions and numbers for specimens of different cross-sections

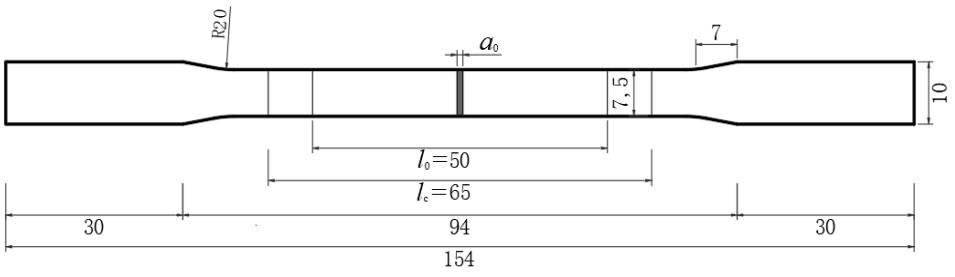

(a) 7.5 mm gauge length width

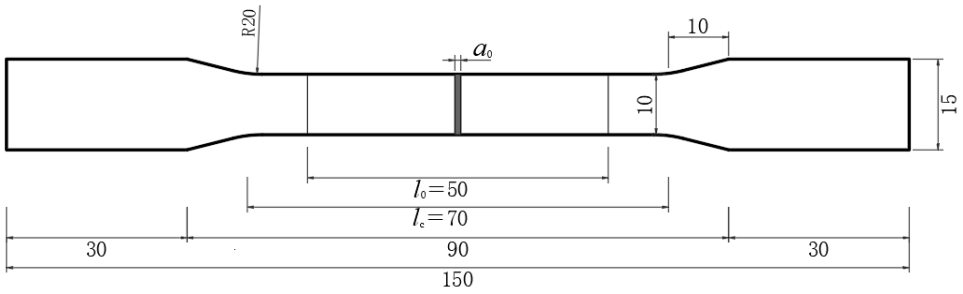

(b) 10 mm gauge length width

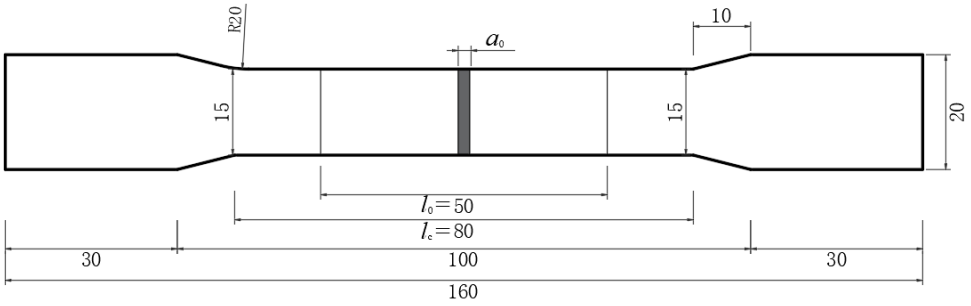

(c) 15 mm gauge length width

Fig. 9 Processing dimensions of different tensile specimens

In Fig. 9, a_0 is the original thickness, l_0 is the original gauge length (l_0=5.56$\sqrt{S_0}$), S_0 is the original cross-sectional area of the parallel length.

Before the start of the experiment, dots are marked on the prepared specimen at intervals of 10mm. They will serve as references for measuring the length after fracture. Material property tests were conducted using a 30t microcomputer-controlled electro-hydraulic servo universal testing machine, some representative specimens used in the experiment are shown in Fig. 10.

Fig. 10 Specimens taken from different positions

The tensile deformation of the specimen was measured using an extensometer with a gauge length of 50mm to determine the elastic modulus, as shown in Fig. 11. Further insights into the functional mechanisms of extensometers are available in reference [46].

Fig. 11 Using an extensometer to measure tensile deformation

Before material yielding, the loading speed was set at 1.0 mm/min to observe the material's elastic behavior and stress-strain relationship. After material yielding, the loading speed was appropriately increased to 2mm/min to observe the material's plastic flow and hardening behavior. The increase in loading speed was controlled within a range that does not cause dynamic effects (such as vibration or impact), as these effects could affect the accuracy of the experimental results. As shown in Fig. 12, after the specimen is broken, the length of the fully deformed region is measured using a vernier caliper to calculate the elongation of the specimen.

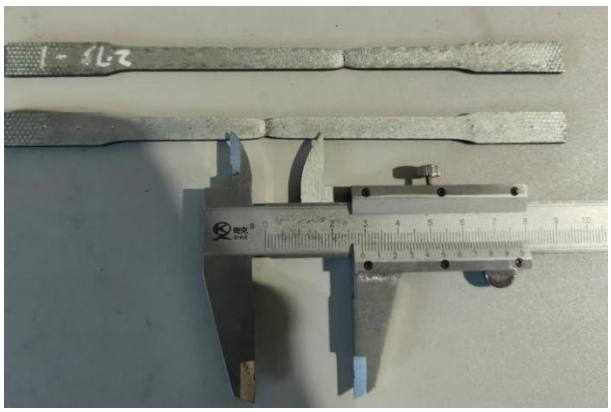

Fig. 12 Measurement of steel elongation

The dimensions a and b are measured using a radius gauge, and the average of a and b-t is calculated as the thickness a value of the specimen. Since the tensile yield strength of the steel profile is essentially equal to its compressive yield strength, if the verification formula is applicable to the tensile yield strength, then the formula is also applicable to the compressive yield strength. The parameters of the CFTWS are shown in Table 1. After three measurements, the data are averaged if all are valid. The comparison of the corner yield strength is shown in Table 2.

Table 1
Parameters of the CFTWS

Thickness	Parameter	Symbol	Value
2.0mm	The strain at a gauge length that is 5 times the diameter	δ_5	39.1%
	The strain at a gauge length that is 10 times the diameter	δ_{10}	32.6%
	The yield strength of the flat plate	σ_s	348MPa
2.75mm	The strain at a gauge length that is 5 times the diameter	δ_5	36.2%
	The strain at a gauge length that is 10 times the diameter	δ_{10}	30.4%
	The yield strength of the flat plate	σ_s	345MPa

Table 2
Comparison of theoretical and experimental yield strengths at the corner

Thickness	a/t	Experimental value	Eq.(27)	Relative error
2.0mm	1.81	448.0MPa	433.9MPa	3.25%
2.75mm	1.65	428.2MPa	423.6MPa	1.10%

Table 2 shows that the theoretical analysis aligns well with the experiments. The yield strength measured using specimens of two different thicknesses has an error range of less than 5%. Moreover, the theoretical calculation results obtained are slightly smaller than the experimental results, which is more conservative. Applying the theoretical formulas from this study in practical engineering can ensure a certain safety margin.

It can be seen that the cold bending effect has a significant impact on the steel. The yield strength of the corner part is about 79-86 MPa higher than that

of the flat part. For the CFTWS used in the prefabricated support and hanger, the yield strength of the corner part can be increased by 23% to 25% compared to the flat part, which has good utilization value. The theoretical formulas have higher precision when the steel plate thickness is larger. On one hand, the degree of anisotropy of thick steel plates is relatively low [47], which can better meet the assumptions in the theoretical formulas, thereby making the theoretical calculation results closer to the experimental values. On the other hand, the error in measuring the value of for thick steel plates is smaller, which in turn improves the accuracy of the calculation results.

In addition, it can be observed that in the same batch of steel produced by the same cold bending process, the yield strength of CFTWS sections slightly decreases with the increase of thickness, and thinner steel plates exhibit higher yield strength. This is because when the steel plate thickness is thinner, the degree of deformation the material undergoes during the cold bending process is greater, making it more prone to work hardening, which significantly increases the yield strength. When thin steel plates are bent, the stress distribution on their cross-section is more concentrated, and the deformation per unit area is greater, leading to more dislocations moving and accumulating in the crystal lattice, hindering further plastic deformation, and thereby significantly enhancing the material's strength.

5. Numerical simulation

Taking the tensile specimen corresponding to position 2-1 as an example, the geometric model shown in Fig. 9 (a) is established using the ABAQUS software. In the "Property" module, the material properties of Q345 CFTWS are defined, including the elastic modulus (210 GPa), Poisson's ratio (0.3), etc. The plastic parameters are inputted based on the curve shown in Fig. 13, which is obtained from the experiment.

In the "Mesh" module, the solid element type is selected to mesh the model, and the approximate global size is set to 0.5. This size is chosen based on experience from similar simulations. It's fine enough to capture key structural behavior details without excessive computational cost. The 0.5mm mesh balances computational efficiency and result accuracy. No significant changes in key response variables are observed with further refinement, indicating satisfactory convergence for this study. After the meshing of the specimen is completed, it is shown in Fig. 14. The hexahedral mesh quality is good, with regular element shapes, no obvious distortion, and the Jacobian value is close to 1.

In the "Step" module, the options "Large deformation" and "Nonlinear geometry" are selected to simulate the yielding behavior of the material. In the "Interaction" module, two reference points are established at the centroid positions of the cross-sections at both ends of the specimen, and the sections are coupled with the reference points through the coupling command. In the "Load" module's "Boundary Condition Manager" tab, a fixed constraint is applied to one end of the specimen to simulate the fixture's clamping. A displacement is applied to the reference point at the other end to simulate the stretching process in the tensile experiment, until the specimen fails and the process stops. The job is submitted in the Job module, and after the calculation is completed, the stress distribution and the development of the plastic zone of the specimen are viewed.

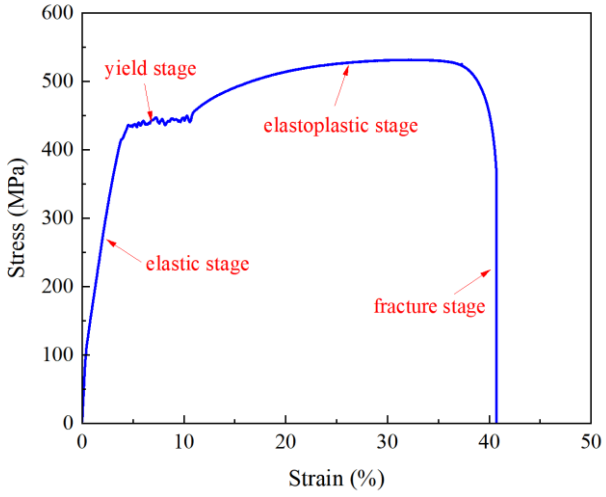

Fig. 13 The stress-strain curve of the steel at position 2-1

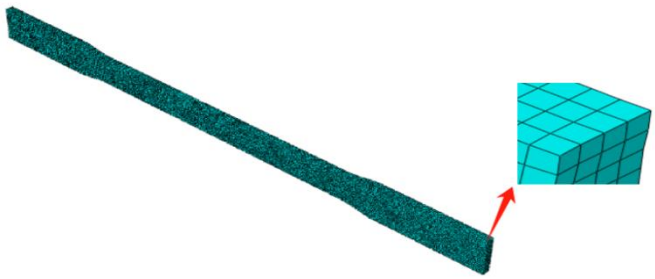

Fig. 14 The meshing of the specimen

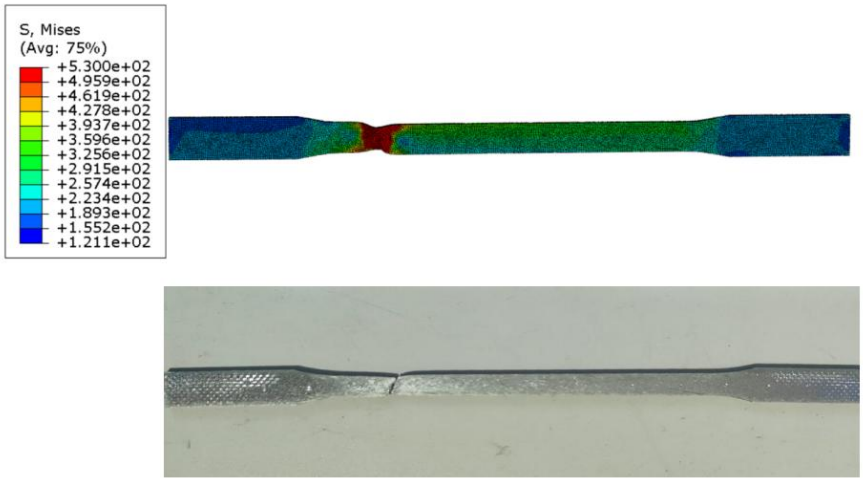

Fig. 15 Comparison between ABAQUS simulation and experiment at position 2-1

The numerical simulation in Fig. 15 shows the stress data during corner material failure aligns with Fig. 13, especially for maximum tensile stress, indirectly proving the theory's feasibility. Additionally, the failure state of the specimen obtained through ABAQUS calculation is basically consistent with the experimental failure state. The high degree of coincidence between the two validates the correctness and effectiveness of the research findings in this study.

In line with the previous research approach, position 2.75-1 was selected for validation. The comparison results are shown in Fig. 16. After changing the thickness of the CFTWS, the failure mode experiments and ABAQUS simulations still show high consistency. This addition further validates the accuracy of the theoretical model across different locations, demonstrating the robustness of this study.

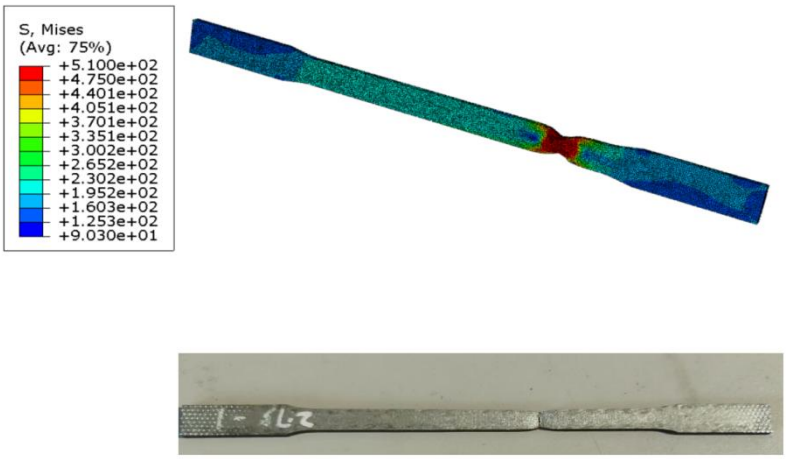

Fig. 16 Comparison between ABAQUS simulation and experiment at position 2.75-1

6. Conclusions

This paper derives the yield strength calculation formula for the corner parts of CFTWS used in prefabricated support and hanger by employing a linear strengthening model. The stress analysis is conducted and the corresponding mechanical model is established based on the idea that the yield stress at each point of the corner part is equal to the effective stress at that point during the cold forming process. The validity of the theory is verified by experimental data and finite element results. The key findings are as follows:

(1) The theoretical formula in this study has a clear physical meaning and good calculation accuracy. Compared with the experimental results, the calculation error of the yield strength for the corner parts is within 5%.

(2) The CFTWS is significantly affected by the cold forming effect. The yield strength of the corner parts is about 23% to 25% higher than that of the flat parts, which has good utilization value.

(3) Due to the influence of theoretical assumptions and actual thickness measurement, the theoretical formula of this study has higher calculation accuracy when the steel plate thickness is larger.

(4) Under the same conditions, the yield strength of thin steel plates is more sensitive to the cold forming process. Because the deformation per unit area is greater during bending, more dislocations move and accumulate in the lattice, making it easier for the yield strength to increase.

The next step of the research will employ the power-law strengthening model to study the yield strength of the cross-section, taking into account the influence of initial imperfections. A yield strength modification coefficient considering the cold forming strengthening effect will be proposed, and it is suggested that relevant content be added to the specifications to expand the scope of application of the theory.

References

[1] Luo T, Xue X, Wang Y, et al. A systematic overview of prefabricated construction policies in China[J]. Journal of Cleaner Production, 2021, 280: 124371.
[2] Zhong R Y, Peng Y, Xue F, et al. Prefabricated construction enabled by the Internet-of-Things[J]. Automation in Construction, 2017, 76: 59-70.
[3] Tam V W Y, Tam C M, Zeng S X, et al. Towards adoption of prefabrication in construction[J]. Building and environment, 2007, 42(10): 3642-3654.
[4] Navaratnam S, Satheeskumar A, Zhang G, et al. The challenges confronting the growth of sustainable prefabricated building construction in Australia: Construction industry views[J]. Journal of Building Engineering, 2022, 48: 103935.
[5] Adanur Ö, Varol F. Investigation of the effect of friction force on the energy absorption characteristics of thin-walled structures loaded with axial impact force[J]. Materials Today Communications, 2023, 36: 106420.
[6] Wang X T Z, PLi L J L, NSu X P W, et al. Restoring force model of phosphogypsum-filled cold-formed thin-walled square steel tube composite wall[J]. Materials Today Communications, 2024, 65.
[7] Magnucka-Blandzi E, Magnucki K. Buckling and optimal design of cold-formed thin-walled beams: Review of selected problems[J]. Thin-Walled Structures, 2011, 49(5): 554-561.
[8] Kawasaki M, Lee H J, Jang J, et al. Strengthening of metals through severe plastic deformation[J]. Reviews on Advanced Materials Science, 2017, 48(1).
[9] Zhuravlev G M, Gvozdev A E, Cheglov A E, et al. Maximum plastic strengthening in tool steels[J]. Steel in Translation, 2017, 47: 399-411.
[10] Wang Z, Shi S, Yu J, et al. Enhanced cryogenic tensile properties through cryogenic cyclic plastic strengthening in a metastable austenitic stainless steel[J]. Scripta Materialia, 2023, 222: 115024.
[11] Key P W, Hancock G J. A theoretical investigation of the column behaviour of cold-formed square hollow sections[J]. Thin-Walled Structures, 1993, 16(1-4): 31-64.
[12] Chen M T, Young B. Material properties and structural behavior of cold-formed steel elliptical hollow section stub columns[J]. Thin-Walled Structures, 2019, 134: 111-126.
[13] Tong L, Hou G, Chen Y, et al. Experimental investigation on longitudinal residual stresses for cold-formed thick-walled square hollow sections[J]. Journal of Constructional Steel Research, 2012, 73: 105-116.
[14] Young B, Lui W M. Behavior of cold-formed high strength stainless steel sections[J]. Journal of Structural Engineering, 2005, 131(11): 1738-1745.
[15] Zheng B, Shu G, Jiang Q. Experimental study on residual stresses in cold rolled austenitic stainless steel hollow sections[J]. Journal of Constructional Steel Research, 2019, 152: 94-104.
[16] Cruise R B, Gardner L. Residual stress analysis of structural stainless steel sections[J]. Journal of constructional steel research, 2008, 64(3): 352-366.
[17] Wang S, Xue H, Cui Y, et al. Effect of Different Cold Working Plastic Hardening on Mechanical Properties of 316L Austenitic Stainless Steel[J]. Procedia Structural Integrity, 2018, 13: 1940-1946.
[18] Byun T S, Hashimoto N, Farrell K. Temperature dependence of strain hardening and plastic instability behaviors in austenitic stainless steels[J]. Acta Materialia, 2004, 52(13): 3889-3899.
[19] Ghosh S, Kain V. Effect of surface machining and cold working on the ambient temperature chloride stress corrosion cracking susceptibility of AISI 304L stainless steel[J]. Materials Science and Engineering: A, 2010, 527(3): 679-683.
[20] Kim J S, Kim J K. Martensitic-transformation-driven strain-softening in the cryogenic deformation of austenitic stainless steel[J]. Materials Science and Engineering: A, 2024: 147681.
[21] Macdonald M, Taylor G T, Rhodes J. The effect of cold forming on the yield strength of thin gauge steel—hardness test approach[J]. Thin-Walled Structures, 1997, 29(1-4): 243-256.
[22] Ungureanu V, Kotełko M, Mania R J, et al. Plastic mechanisms database for thin-walled cold-formed steel members in compression and bending[J]. Thin-Walled Structures, 2010, 48(10-11): 818-826.
[23] Yao Y, Quach W M, Young B. Finite element-based method for residual stresses and plastic strains in cold-formed steel hollow sections[J]. Engineering Structures, 2019, 188: 24-42.
[24] Yao Y, Quach W M, Young B. Simplified models for residual stresses and equivalent plastic strains in cold-formed steel elliptical hollow sections[J]. Thin-Walled Structures, 2020, 154: 106835.
[25] Luo K, Li H, Yang J, et al. Research on post-fire mechanical properties of thin-walled cold-formed steel and its influence on the Σ-shaped columns after fire exposure[J]. Thin-Walled Structures, 2024, 204: 112315.
[26] Kim J W, Lee M Y, Lee S Y. Estimation of Tensile Properties of Pipe Bends Manufactured by Cold-Bending[J]. Transactions of the Korean Society of Mechanical Engineers A, 2012, 36(9): 1059-1064.
[27] Korsun N, Prostakishina D. Modeling thin-walled elements with regard to steel hardening[C]//E3S Web of Conferences. EDP Sciences, 2021, 263: 02044.
[28] Gao T, Moen C D. The cold work of forming effect in steel structural members[J]. SDSS' Rio 2010 stability and ductility of steel structures, 2010: 1017-1024.
[29] Roy A M, Guha S. A data-driven physics-constrained deep learning computational framework for solving von Mises plasticity[J]. Engineering Applications of Artificial Intelligence, 2023, 122: 106049.
[30] Barber J R. Plane strain and plane stress[M]//Elasticity. Cham: Springer International

Publishing, 2023: 41-49.
[31] Han J, Matsubara S, Moriguchi S, et al. Variational crack phase-field model for ductile fracture with elastic and plastic damage variables[J]. Computer Methods in Applied Mechanics and Engineering, 2022, 400: 115577.
[32] Bechir H, Mendil F, Yaya K. Extension and inflation of a thick-cylindrical tube made of isotropic compressible of Mooney-Rivlin materials: modeling and finite element simulations[J]. Acta Mechanica, 2023, 234(11): 5461-5475.
[33] Zhang Y, Cai J, Mi C, et al. Effect of surface residual stress and surface layer stiffness on mechanical properties of nanowires[J]. Acta Mechanica, 2022: 1-25.
[34] Zhang X, Li Y, Lei J, et al. Time-dependent effects of microplastics on soil bacteriome[J]. Journal of Hazardous Materials, 2023, 447: 130762.
[35] Lee E H, Rubin M B. Eulerian constitutive equations for the coupled influences of anisotropic yielding, the Bauschinger effect and the strength-differential effect for plane stress[J]. International Journal of Solids and Structures, 2022, 241: 111475.
[36] Patra A K, Kapoor R, Mandal S, et al. Influence of strain rate on the work hardening, strain induced martensite formation, strain partitioning, and variant selection in a medium-Mn steel[J]. Materials Science and Engineering: A, 2024, 902: 146593.
[37] Camotim D, Basaglia C. On the behaviour, failure and direct strength design of thin-walled steel structural systems[J]. Thin-Walled Structures, 2014, 81: 50-66.
[38] Liu S W, Liu Y P, Chan S L. Direct analysis by an arbitrarily-located-plastic-hinge element—Part 1: Planar analysis[J]. Journal of Constructional Steel Research, 2014, 103: 303-315.
[39] Rasmussen K J R, Hancock G J. Design of cold-formed stainless steel tubular members. II: Beams[J]. Journal of Structural Engineering, 1993, 119(8): 2368-2386.
[40] Ban H, Yao Y. The coupling effects of strain gradient and damage on Mode I crack tip stress fields[J]. Theoretical and Applied Fracture Mechanics, 2023, 126: 103989.
[41] Qin F, Wei X, Lu Y, et al. Flexural behaviour of high strength engineered cementitious composites (ECC)-reinforced concrete composite beams[J]. Case Studies in Construction Materials, 2023, 18: e02002.
[42] Liu S W, Liu Y P, Chan S L. Direct analysis by an arbitrarily-located-plastic-hinge element—Part 2: Spatial analysis[J]. Journal of Constructional Steel Research, 2014, 103: 316-326.
[43] Liu S W, Liu Y P, Chan S L. Advanced analysis of hybrid steel and concrete frames:Part 1: Cross-section analysis technique and second-order analysis[J]. Journal of Constructional Steel Research, 2012, 70: 326-336.
[44] Liu S W, Liu Y P, Chan S L. Advanced analysis of hybrid steel and concrete frames: Part 2: Refined plastic hinge and advanced analysis[J]. Journal of Constructional Steel Research, 2012, 70: 337-349.
[45] Metallic materials-Method of test at room temperature: GB/T228-2002[S]. Beijing: China Standards Press, 2002. (in Chinese)
[46] Alias M A, Ismail M F, Sa'ad M S M, et al. A high-precision extensometer system for ground displacement measurement using fiber Bragg grating[J]. IEEE Sensors Journal, 2022, 22(9): 8509-8521.
[47] Meyers M A, Chawla K K. Mechanical behavior of materials[M]. Cambridge university press, 2008.